

Effect of Additively Manufactured Wall Lattice Structures on Flashback Limits in a Hydrogen Jet Flame Combustor

Alexander Jaeschke^{*1}, Thomas Ludwig Kaiser², Lukas Melzig³, Michael F. Zaeh³, Kilian Oberleithner², and Christian Oliver Paschereit¹

¹Chair of Fluid Dynamics – Technische Universität Berlin, Germany

²Laboratory for Fluid Instabilities and Dynamics – Technische Universität Berlin, Germany

³Institute for Machine Tools and Industrial Management (*iwb*) – Technical University of Munich, Germany

Keywords— gas turbine, hydrogen combustion, jet flame, flashback, PIV, additive manufacturing, PBF-LB/M

arXiv:2606.12302v1 [physics.flu-dyn] 10 Jun 2026

^{*}a.jaeschke@tu-berlin.de

Abstract

This study investigated how additively manufactured nozzles with body-centered cubic lattice structures reduce the flame flashback propensity in a hydrogen jet flame burner. Five different configurations of a jet flame combustor were investigated, with a focus on mixing duct walls incorporating porous media. The nozzles were manufactured by the powder bed fusion of metals using a laser beam process. The lattice parameters were varied by the volume fraction and the strut diameter. For the experiments, pure hydrogen was used as fuel under atmospheric conditions at various equivalence ratios and Reynolds numbers of 9,000 – 12,000. Flow field measurements, flame imaging, and spectral proper orthogonal decomposition of the flame dynamics were employed to identify possible transition mechanisms from a stable operation to flashback. The flow fields and the flame shapes showed only minor effects from wall modifications, preserving general flow characteristics across configurations. The flow dynamics in the combustion chamber were dominated by large-scale coherent structures in the shear layer, specifically Kelvin-Helmholtz instabilities. The results demonstrated that the nozzle with the coarsest porous wall structure significantly improved the flashback resistance compared to a nozzle with a solid wall. It is concluded that the primary mitigation mechanism was a cooling effect by unburnt mixture flowing through the porous media. The findings confirmed that the integration of lattice structures through additive manufacturing provides a viable strategy for hydrogen flashback mitigation by manipulating the coupled interaction between the flame and the thermal conditions of the wall.

Introduction

Hydrogen presents both significant promise in carbon dioxide reduction and substantial engineering challenges for the combustion in gas turbines. As renewable energy sources increasingly dominate the energy sector to replace fossil fuels, unpredictable fluctuations and seasonal availability variations emerge. Gas turbines offer an efficient way to enhance the flexibility in renewable energy-based power systems. To maintain low carbon emissions, hydrogen is the preferred alternative to replace natural gas as fuel. However, the high reactivity and flame temperature of hydrogen allow only limited quantities in fuel mixtures before flame flashback (FB) occurs in swirl-stabilized industrial gas turbines [12, 14, 25].

Increasing the axial velocity prevents the flame propagation upstream into regions which are not designed to withstand flame anchoring. Jet-stabilized flame concepts therefore represent a promising solution for hydrogen combustion [22, 28, 30, 33]. Fully exploiting the potential of hydrogen requires addressing flame flashback, nitrogen oxide (NO_x) emissions, and dynamic instability. Additive manufacturing (AM) has the potential to make a substantial contribution to overcome these challenges due to the significant design freedom it offers [30, 35, 34].

For turbulent hydrogen jet flames, boundary layer FB is the dominant mechanism [7, 3]. The interaction of the inlet velocity, the turbulent flame speed, and the flame quenching distance can cause the flame to propagate upstream along the wall when the boundary layer velocity falls below the burning velocity in proximity to the wall, known as the critical gradient concept [1, 7]. Recent studies draw a more complex picture of the process revealing that velocity fluctuations initiate the onset of FB [39, 38] and that backflow regions form ahead of the FB propagating into the mixing tube [3, 19]. Thereby, the elevated burning velocity of hydrogen stems not solely from its higher laminar flame speed but also

from thermal-diffusive instability [24], which drives the characteristic conical shape of the flame across a wide range of operating conditions.

Studies by Duan et al. [5] and Baumgartner et al. [6] reported a strong influence of the burner material, the flame confinement, and the burner tip temperature on the FB propensity. They proposed burner rim cooling to prevent FB but also suggested low-conductivity injector material or coatings for an improved thermal stability. Based on these results and comprehensive FB measurements a low-order model was proposed by Kalantari et al. [9] but it cannot reliably predict FB limits with parameters far from the initial conditions. Significant improvements were done by Hoferichter et al. [8] but the transferability to other configurations is still a limiting factor.

Park et al. [38] reevaluated in their recent study the influence of the wall heat flux and its relationship to FB dynamics for an unconfined jet flame burner. They confirmed the findings of Duan et al. [5] with a more detailed look at the quantification of the wall heat flux and the resulting quenching distance for different burner cooling strategies. They stated that a comparison with data from the literature is only possible on a qualitative basis revealing the critical influence of trivial adjustments and setup details in FB studies.

Strategies for the detection of FB in a single-jet hydrogen burner were reported by zur Nedden et al. [37] aiming for a reliable method for early FB detection with promising results based on measurements of the material resistance at the mixing tube rim.

Ax et al. [34] reported on a single-nozzle configuration and its feasibility of operating with 100 % hydrogen at gas turbine relevant conditions. They stated that the transferability of the reported FB limits to full-scale multi-nozzle gas turbine burner might be difficult because of the influence of adjacent flames. Key aspects identified in the study were the surface roughness of the mixing duct and a local increase in the heat transfer on the nozzle rim.

Investigations on multi-jet burners confirmed the potential of jet-stabilized combustion systems composed of individual single jets. FB limits, NO_x emissions, and dynamic stability were investigated for various setups reporting promising results for hydrogen combustion [28, 27, 21, 20]. Full-engine tests of a piloted multi-nozzle combustor under full-load conditions were recently published by Hermeth et al. [30]. The reported fuel-flexible system was capable of operating with 100 % hydrogen showing promising results on the flame stability, emissions, and the FB risk. However, the tests were limited by head-end temperature constraints imposed by the FB risk. Progress in reaching full-load conditions with 100 % hydrogen were also reported by [40].

Despite intense research, many questions on the onset of FB are still unclear. Recent investigations by von Saldern et al. [42] identified low-frequency streaky structures in a lean hydrogen flame raising the question of how jet dynamics impact the FB behavior.

The present study investigated additively manufactured nozzle designs for hydrogen flame FB mitigation in jet flame burners, with a focus on mixing duct walls incorporating porous media. The central question was to what extent the porous wall sections increase the FB resistance and what the dominant underlying mechanism is. Nozzle variants were compared under both stable and unstable operating conditions, and were evaluated against known FB indicators, such as the burner rim temperature. Flow field measurements and flame imaging were used to characterize the influence of porous media on the combustion process, while flow dynamics were analyzed to identify possible transition mechanisms from a stable operation to FB.

1 Materials and methods

1.1 Experimental setup

In this study, five different configurations of jet flame burners were investigated by modifying the upper mixing duct section, called nozzle. The AM nozzles were made of Inconel 718 and comprised three different variants with a porous wall section, shown in Fig. 1, and one solid variant without porous media. The porous section had an axial length of 40 mm and a radial thickness of 4 mm. All AM porous nozzles had a solid outer wall in the radial direction. In the axial direction, the porous section ended with a solid plate 1 mm thick at the nozzle outlet, which was flush with the burner plate and covered the porous area of the combustion chamber. Therefore, the entire gas mixture passed through the nozzle outlet into the combustion chamber. For a comparison with conventionally manufactured nozzles and data from the literature, one nozzle, geometrically identical to the solid AM nozzle, was machined from 304 stainless steel (1.4301).

The porosity in the wall areas was realized through the integration of body-centered cubic (BCC) lattice structures into the nozzles. These lattice structures were characterized by their volume fraction V_f , their strut diameter d_{strut} , their surface area A_{cell} , and the resulting pore size d_{pore} , which is the free spacing between the lattice struts. The volume fraction is defined as the proportion of solid material within the total volume of a lattice structure. The surface area ratio, relative to a plain wall element of identical outer dimensions, is given by a constant of $A_{\text{cell}}/A_{\text{solid}} = 4$. The naming of each nozzle in this study is based on its strut diameter and volume fraction, for example N-950 with $d_{\text{strut}} = 0.9$ mm and $V_f = 50$ %. An overview of the dimensions of the lattice structures is given in Tab. 1.

Table 1: Overview of the dimensions of the lattice structures

	V_f (-)	d_{strut} mm	d_{pore} mm	A_{cell} mm ²	$A_{\text{cell}}/A_{\text{solid}}$ (-)
N-350	50	0.3	0.4	2.6	4
N-330	30	0.3	0.6	3.9	4
N-950	50	0.9	1.1	23.2	4

1.2 Manufacturing of the AM nozzles

For the manufacturing of the nozzles, the powder bed fusion of metals using a laser beam (PBF-LB/M) process was employed. In this process, the part is manufactured incrementally by selectively fusing powder layers by a focused laser beam [18]. All nozzle specimens were manufactured in a single pass on an EOS M400-1 PBF-LB/M machine (EOS GmbH, Germany) from the nickel-based superalloy Inconel 718 (Oerlikon Metco Europe GmbH, Germany). This machine was equipped with a 1 kW continuous-wave Yb fiber laser with a wavelength of 1064 nm. To minimize the influence of process-related effects, which were not investigated in this study, the specimens were arranged randomly on the build platform, which was kept at a constant temperature of 353 K during the manufacturing process. To maintain an inert atmosphere within the process chamber and prevent high-temperature oxidation of the molten metal, 99.999 % pure Argon was used. While the geometry of the lattice structures was changed, all nozzle specimens were manufactured using the standard process parameters for Inconel 718. The laser power P was set to 285 W, the scan speed v to 960 mm/s, the hatch distance h to 110 μm , and the layer thickness d_L to 40 μm . A non-patterned line exposure with a rotation of 67° between two subsequent layers was selected as the scan pattern. The manufacturing process was followed by several post-processing steps, including the thorough cleaning of the specimens, the machining of the functional surfaces, and

the drilling of holes for the integration of various sensors.

Since, in addition to the different lattice structures in the nozzle wall, the material properties also influence the combustion process, Fig. 2 illustrates the differences in the thermal conductivity κ between the two tested nozzle materials as a function of the temperature T .

1.3 Test rig

The atmospheric jet flame test rig, shown in Fig. 3, comprised a premixed hydrogen-air mixture entering through six circumferential inlets at the burner base. Mass flow controllers regulated the fuel and air with an accuracy of $\pm 0.2\%$. The mixture passed through a metal sinter plate with a pore size of $25\ \mu\text{m}$ to prevent flame FB into the supply lines, then entered the settling chamber where seeded air was added for the particle image velocimetry (PIV) measurements. The AM mixing duct contained a thermocouple (TC) at its entrance to detect flame FB. A detected temperature rise by a flame moving unintentionally upstream into the mixing duct section triggered an automatic shutdown. A 1 mm thick zig-zag structure (see Fig. 4) was positioned 100 mm upstream of the combustion chamber outlet to promote a rapid transition to a turbulent flow.

The flame anchored close to the mixing duct outlet inside the 300 mm long quartz glass combustion chamber with an open outlet. The inlet temperature of the unburnt mixture was 293 K.

The upper mixing duct section (indicated by the green area in Fig. 4) was changeable and accommodated the different AM nozzles as described in Sec. 1.1. All nozzles had an outlet diameter of $d = 20\ \text{mm}$. The burner flange had internal air cooling with a constant cooling mass flow of 8 kg/h and an inlet temperature of 293 K.

Five differential pressure sensors (1000 Pa range, 100 μs response time) were positioned along the mixing duct wall at a spacing of $0.5d - 0.8d$, starting 2.5 mm downstream of the combustion chamber. Daily zero-offset calibration was performed. Stable operating points were sampled at 15 kHz and FB points at 10 kHz both evaluated over 3 seconds. The power spectra were calculated using the Welch method with a Hanning window, a segment length of 2500 samples, and a window overlap of 50 %. This resulted in a frequency resolution of 0.33 Hz. Savitzky-Golay filtering was utilized for noise reduction. The Nyquist frequency was set to half the sample rate. Six type-K thermocouples with a diameter of 1 mm were flush-mounted circumferentially at the nozzle outlet, 1.2 mm upstream of the combustion chamber, shown in Fig. 4. Thermocouple and mass flow data were acquired for 30 seconds at a sampling frequency of 10 Hz.

1.4 Operating conditions

An overview of the operating conditions tested in this study is presented in Tab. 2.

Table 2: Overview of the operating conditions

	\dot{m}_{air} kg/h	\bar{u}_x m/s	ϕ (-)
stable	10; 13	9; 11.5	0.39; 0.44; 0.48
FB test	8; 10; 12	8.5; 9; 11	0.44 – 0.6

The air mass flows \dot{m}_{air} under stable operating conditions were investigated for three equivalence ratios ϕ unless FB occurred beforehand, corresponding to calculated adiabatic flame temperatures T_{ad} of 1400 K, 1500 K, and 1600 K. The thermal power ranged from 3.7 kW to 7 kW depending on the conducted air mass flow and equivalence ratio. The flame

properties were calculated using the CANTERA chemical kinetics solver [10] and the GRI 3.0 mechanism [43]. Reynolds numbers at the mixing duct outlet ranged from 9,000 – 12,000 depending on the operating condition, calculated using the bulk velocity \bar{u}_x of the unburnt hydrogen-air mixture and the nozzle outlet diameter d .

Flashback, defined as the upper stability limit of the burner where the flame unintentionally enters the mixing duct and moves upstream, was triggered using a controlled procedure. While the air mass flow remained constant, the flame temperature was increased in small increments ΔT_{ad} of 10 – 15 K by raising the hydrogen mass flow. After each increment, the thermal equilibrium indicated by the temperature sensors was awaited before the next increase of the fuel mass flow. When a FB occurred, the thermocouple inside the combustor detected the temperature rise from the upstream flame position, automatically shutting down the test rig. This feedback control loop (≈ 2 seconds response time) prevented damage to the equipment. A cool down period of 10 minutes followed each shutdown to ensure identical initial conditions for each measurement. The procedure achieved a high repeatability, with deviations of 0.64 – 0.83 % of the calculated adiabatic flame temperature which is within the range of the incremental temperature increase ΔT_{ad} used to trigger the FB. For technical reasons, the higher air mass flow of $\dot{m}_{\text{air}} = 13$ kg/h had to be reduced to $\dot{m}_{\text{air}} = 12$ kg/h for the FB tests with the procedure remaining the same.

1.5 Optical measurements

The PIV laser sheet entered the combustion chamber from the downstream end through a mirror angled at 90° above the outlet (Fig. 3), minimizing interfering reflections on the quartz glass walls. An air stream cooled the mirror and deflected hot exhaust gases to prevent overheating. The image regions covered by the cameras are highlighted in Fig. 4.

The PIV system employed a double-pulse Nd:YAG laser ($\lambda = 532$ nm, 10 kHz repetition rate) with a pulse separation of $\Delta t = 100$ μs , which was kept constant across all measurements to ensure an adequate particle displacement between the snapshots. Zirconium dioxide particles ($d_{\text{ZrO}_2} = 0.5$ μm) were seeded 600 mm upstream of the combustion chamber outlet by an seeding air mass flow of 2 kg/h, independent of the actual combustion air mass flow \dot{m}_{air} . The seeding mass flow was taken into account in the calculations.

Mie scattering was detected by a Photron SA-1.1 CMOS high-speed camera with a 532 nm bandpass filter. The measurement area covered 80 mm \times 200 mm around the mixing duct outlet with a sheet thickness of 1.5 mm. The PIV snapshots were recorded with a resolution of 5.8 px/mm. For each measured case 23,000 snapshots were recorded that yield a record length of 2.3443 s. Post-processing employed standard PIV techniques with a 16 px \times 16 px multi-grid interrogation window at 81 % overlap resulting in 200 \times 166 grid points for the calculated velocity field.

Flame imaging was performed using line-of-sight OH*-chemiluminescence measurements. The OH* radical provides a qualitative indication of the heat release zone, representing the flame front, as was shown by [32]. An intensified Photron SA-Z CMOS high-speed camera equipped with a bandpass filter with a wavelength of $\lambda = 310$ nm recorded at 10 kHz with a spatial resolution of 7.8 px/mm. PIV and flame imaging was conducted synchronously. The imaging was triggered by the PIV camera for a temporal synchronization, which resulted in an identical acquisition time and number of snapshots. Mean flame images were acquired separately using a bandpass-filtered sCMOS camera with an exposure time of 0.8 s and a spatial resolution of 9.5 px/mm.

1.6 Spectral proper orthogonal decomposition

To identify coherent structures within the turbulent flow, spectral proper orthogonal decomposition (SPOD) was applied to the PIV snapshots. SPOD, unlike space-only POD, operates in the frequency domain to extract structures that are coherent both in space and in time, allowing for the analysis of flow dynamics. A more detailed explanation can be found in the work of [15]. Typically, SPOD is applied to the fluctuating component of a variable, so the mean is first subtracted from each snapshot before the analysis

$$\mathbf{q}' = \mathbf{q} - \bar{\mathbf{q}}, \quad (1)$$

where \mathbf{q} is the state vector at a given time instance and contains the information of the PIV snapshot. With the prime and overline symbol the fluctuating and the time-averaged component is denoted, respectively. In the following step, temporal blocks of the fluctuating quantity are Fourier-transformed. The Fourier amplitudes of all blocks are stacked in a matrix for the respective frequencies

$$\hat{\mathbf{Q}}_\omega = \left[\hat{\mathbf{q}}_\omega^{(1)} \quad \hat{\mathbf{q}}_\omega^{(2)} \quad \hat{\mathbf{q}}_\omega^{(3)} \quad \dots \quad \hat{\mathbf{q}}_\omega^{(N_B)} \right], \quad (2)$$

where $\hat{\mathbf{q}}_\omega^{(j)}$ denotes the complex Fourier amplitude at the temporal frequency ω obtained from block j . The number of blocks is denoted N_B and depends on the length of the time series, the length of the individual blocks and their selected overlapping. Based on $\hat{\mathbf{Q}}_\omega$, the cross spectral density matrix is determined, whose eigenvectors are the SPOD modes

$$\frac{1}{N_B - 1} \hat{\mathbf{Q}}_\omega \hat{\mathbf{Q}}_\omega^H \hat{\Psi}_\omega = \hat{\Psi}_\omega \hat{\Lambda}_\omega. \quad (3)$$

The superscript H denotes the complex conjugate transpose. The columns of $\hat{\Psi}_\omega$, denoted $\hat{\psi}_\omega^{(j)}$ are the SPOD modes and the elements of the diagonal matrix $\hat{\Lambda}_\omega$, denoted $\lambda_\omega^{(j)}$ are the corresponding SPOD eigenvalues. The SPOD modes are orthonormal, and for each mode, the energy is given directly by its eigenvalue. High-energy modes are particularly relevant for the flow dynamics and the modes are therefore ordered by decreasing eigenvalue such that the first mode, with eigenvalue $\lambda_\omega^{(1)}$, is the most energetic. If this leading mode contains substantially more energy than the subsequent modes, the spectrum is said to exhibit low-rank behavior, meaning that the dynamics at that frequency are dominated by the first mode.

In the following, the axial and transverse velocity components from PIV were analyzed with SPOD. For the velocity, the energy is given in units of m^2/s^2 and can be interpreted as a measure for the turbulent kinetic energy, neglecting density variations. For brevity, only the real part of the SPOD modes is shown in the following. To ensure that the amplitude is representative, the real part is displayed at the phase angle at which it was largest.

The length of the PIV time series for the SPOD was reduced to 12,800 snapshots to provide a consistent image number for both stable and unstable operating conditions. To focus the calculation on the flow field region impacted by the flame, the snapshots were cropped in the downstream direction at $x/d = 3.9$. For the decomposition, the number of frequencies was set to $n_{\text{DFT}} = 256$ with an overlap of 50 %, resulting in 49 blocks for the POD.

2 Experimental results

In the following section, the results of the measurements are presented and analyzed. First, the mean flow was analyzed for effects caused by changing the wall structure. Subsequently, the FB behavior was investigated, and finally, the flow dynamics were examined.

2.1 Mean flow

Figure 5 shows the averaged flame images of the line-of-sight integrated OH* signals for the five nozzle variants. The operating point was at an adiabatic flame temperature of $T_{\text{ad}} = 1600$ K and a bulk flow velocity of $\bar{u}_x = 11.5$ m/s.

For all cases, the flames exhibited a typical conical jet shape, with increased OH* intensity along the cone edges due to the line-of-sight integration. The axial position of the flame length l_F was defined by the maximum of the OH* mean intensity integrated over the y -direction. The strongest heat release occurred near the calculated flame length and is accompanied by a thickening of the edge region with high OH* intensity. The length of the flame tends to decrease as the lattice cell size increases (left to right in Fig. 5). A notable decrease in the flame length was observed for the nozzle N-950, which has the coarsest lattice structure. This may result from an increased turbulence by the lattice structures of the walls. Nozzles with porous walls show a slight asymmetry in the heat release in Fig. 5. Evaluated over all measured cases this asymmetry depends on the operating condition and, to some extent, also varied for the nozzles with solid walls.

To address the observed changes in the shape of the flames, Fig. 6 shows the axial mean velocity \bar{u}_x at different downstream positions in the combustion chamber. The operating conditions were identical to those of the OH* images in Fig. 5. The velocity profiles exhibited the typical decay and radial spreading expected for a jet configuration. Apart from small deviations, all measured profiles agreed well and showed comparable velocities.

At $x/d = 2.25$, an increase in the velocity was observed, which can be attributed to the flame position and the associated decrease of the density over the flame front. Toward the combustion chamber wall, the velocity decreased almost to zero. With an area ratio of 25:1 between the burner plate area and the mixing duct outlet area, the burner generated only a very weak recirculation zone in the lower part of the combustion chamber (not shown). The recirculation strengthens once the jet has extended sufficiently to form vortices between the jet and the combustion chamber wall at approximately $x/d = 5$. Nevertheless, the recirculation extended in a narrow band along the shear layer down to the flame root.

The turbulence intensity at the nozzle outlet is shown in Fig. 7, with color coding identical to the previous figure for comparison. The fluctuation velocity u'_{rms} was normalized by the spatial mean of the axial velocity \bar{u}_x , with the evaluation restricted to the nozzle outlet region.

The highest turbulence intensities were measured in the shear layer regions near the nozzle edges ($y/d = \pm 0.5$), decreasing toward the nozzle center. Small differences appeared among the nozzle variants. The machined nozzle showed a high, non-symmetric peak at $y/d = -0.5$, with $u'_{\text{rms},x}/\bar{u}_x = 0.113$, which also represents the largest asymmetry observed. The other nozzles peaked at values ranging from 0.08 – 0.10, consistent with expected values for these experimental conditions [2]. It is concluded that, in contrast to the flame length, no trend related to the lattice structures is observed for the flow field.

2.2 Flashback behavior

After investigating the mean flow under stable flame conditions in the previous section, the focus now shifts to the FB limit of the burner setups.

Figure 8 shows the FB limits, determined using the procedure described in Sec. 1.4. The thresholds are represented by the axial flow velocity as a function of the calculated adiabatic flame temperature, or equivalence ratio, calculated from the last measured mass flows before a FB occurred. Depicted are the five nozzle variations as described in Sec. 1.1 as well as a post-processed version of the solid AM nozzle referred to as *AM refined*, indicated by the red dashed line with the pentagon symbols in Fig. 8. For a better visualization of the trend in the FB data, a linear interpolation between the measured data points was applied. To the left of each interpolated line, stable flame conditions can be assumed. When the flame temperature is increased or the inlet velocity is reduced so that the line is crossed from left to right, the FB limit is reached. All observed FB events were boundary layer FB, confirmed by high-speed imaging.

The highest FB propensity was found for the solid AM nozzle, followed by the nozzle N-350, which had the smallest cell size (finest porous structure). The upper FB limit was shared by the machined nozzle and the nozzle N-950, the latter having the largest cell size of the investigated nozzles. The nozzle N-330 also showed a high FB resistance, but performed worse at a bulk velocity of $\bar{u}_x = 11$ m/s. Therefore, Fig. 8 shows two distinct trends in the FB resistance:

- from low to high thermal conductivity for the solid nozzles with identical geometry
- from small to large cell sizes for the nozzles comprising lattice structures

First, the large gap between the FB limits of the two solid nozzles was investigated. Because the inner surface of the solid AM nozzle was not post-processed, it exhibits the typical surface roughness of this manufacturing method. Typical literature values for the average surface roughness of the AM nozzle material Inconel 718 are $R_a \approx 9$ μm compared to $R_a \approx 1$ μm for stainless steel [31]. The surface roughness can have a very different influence on the FB tendency depending on the material used. Ding et al. [17] conducted a numerical study that observed a decreasing critical velocity gradient with greater wall roughness. This is particularly significant when the material of the wall has a high thermal conductivity, as it results in an increased flame quenching distance due to a greater heat loss. However, flow field modifications in the near-wall region can counteract the effect. Vivoli et al. [41] reported experimental data showing a strong decrease of the FB risk with the increase of the surface roughness utilizing stainless steel mixing tubes.

To exclude the surface roughness as the cause of the observed differences between the two solid nozzles, the solid AM nozzle was post-processed on a lathe to obtain a surface roughness comparable to that of the machined stainless steel nozzle. The reduced surface roughness of the refined AM nozzle slightly increased the FB resistance compared to the solid AM nozzle without treatment of the inner mixing tube wall (see Fig. 8) but this effect was too weak to explain the previously observed gap in the FB risk. It is noted, given the thermal conductivity of Inconel 718 under the tested conditions, that the surface roughness resulting from the manufacturing process is negligible in terms of decreasing the FB propensity.

Since surface roughness effects had been ruled out, the primary difference between the two solid nozzles was the material. Inconel 718 has a thermal conductivity of $\kappa = 11.4$ W/(m·K), which is 25 % lower than the thermal conductivity of 304 stainless steel with $\kappa = 15$ W/(m·K), both at $T = 293$ K (see Fig. 2). Duan et al. [5] have reported that the thermal conductivity strongly influences the FB limits. However, in their cases (brass, quartz glass, and steel), the differences in the thermal conductivity were spanning over one order of magnitude, providing only a qualitative trend relevant to the present study.

To assess the effect of the thermal conductivity on the FB limit, the wall temperature T_{wall} near the mixing duct rim was evaluated, shown in Fig. 9. At stable operating conditions, no clear trend in the wall temperature was observed, which is not shown for brevity. Near FB, the flame anchors closer to the burner rim and exerts the strongest influence on the burner rim temperature. Therefore, the temperature measurements immediately before FB showed distinct separation according to the material of the nozzle. As indicated by the white dashed lines in Fig. 9, the data points of all Inconel 718 nozzles collapse on one line (upper white dashed), while the flashback points of the stainless steel nozzle form another line (lower white dashed). Therefore, it is concluded that the difference in the thermal conductivity caused the observed gap in the FB limits between the solid AM nozzle and the machined nozzle.

Next, the observed trend of the FB limits related to the pore size of the lattice structures is evaluated. In Fig. 9, the quenching distance d_q of the nozzles is shown by the background color coding. The quenching distance was calculated using an empirical formula for hydrogen-air mixtures derived by Kıymaz et al. [36], which incorporates the wall temperature T_{wall} and the equivalence ratio. The quenching distance exhibits a linear trend as a function of the wall temperature, observed in other studies as well [11, 23]. It is noted in Fig. 9 that the calculated quenching distances of the AM nozzles with lattice structure were lower compared to the machined nozzle at the same flame temperature, indicating a higher FB resistance despite the lower thermal conductivity.

Under the present conditions, three potential mechanisms driving the observed FB behavior of the nozzles with lattice structure were identified and will be discussed in the remainder of this study:

- (1) alteration of the mean fields with decreased critical velocity gradient
- (2) passive wall cooling by fresh gases flowing through the lattice structure
- (3) modification of flow dynamics damping flame instability

With regard to the first potential mechanism, it should be noted that the mean flow field data in Sec. 2.1 showed no significant differences between the nozzle variants. For the flame topology, a trend related to pore size was observed where the flame length decreased as pore size increased. Typically, a decreased flame length at identical operating conditions implies an increased turbulent burning velocity, which would theoretically increase FB propensity [8]. However, the opposite was observed here as the FB limit actually increased with shorter flame lengths (and larger pore sizes). This suggests that alteration of the mean fields was not the primary driver of the improved flame stability and rather destabilized the flame.

Instead, the trend in FB limits shown in Fig. 8 directly correlates with the pore size. The lattice structures can significantly enhance the convective heat transfer capability of the wall by the strongly increased surface area. Therefore, a passive wall cooling by the unburnt fresh gases might mitigate FB.

An increased heat transfer of the wall influences the temperature of an unburnt gas mixture T_{unburnt} near the mixing duct wall [11] and thus the state of the flame reactants in proximity to the lattice structures. The results from one-dimensional free flame simulations are presented in Fig. 10. Shown is the unstretched laminar flame speed S_L and the thermal conductivity κ of the fresh gases as a function of the temperature ratio $T_{\text{unburnt}} / T_{\text{ad}}$, respectively. Both values are sensitive to changes in the unburnt gas mixture temperature with a decreasing wall temperature resulting in an increasing quenching distance.

Studies by [17, 41] demonstrated that an increased heat transfer at the wall correlates with FB reduction. However, the penetration depth and turbulence at the cell level are difficult to quantify for the lattice structures. A rigorous investigation would require using numerical simulation for resolving or modeling the porous wall structure, conjugate

heat transfer, reaction modeling, and turbulent flow at $Re = 10,000$, which is outside the scope of this study. However, investigations on the conjugate heat transfer of lattice structures at a comparable Reynolds number and porosity to nozzle N-950 in a rectangular duct, were conducted by Kuwata et al. [13] and Suga et al. [16]. In their numerical and experimental studies, they observed penetration of the fluid into the porous media, accompanied by an increased wall turbulence and an enhanced heat transfer. The rise in turbulence was attributed to Kelvin-Helmholtz (KH) instability developing over the porous wall. Thereby, the nozzle end plate in the present setup is crucial for preventing a reduction in the exit velocity and for supporting flame anchoring, as confirmed by tests with nozzle variants without an end plate, which is not shown for brevity.

As a result, the second hypothesis, i.e. wall cooling by the fresh gases flowing through the lattice structures appears to be a plausible cause for the improved flashback behavior.

Besides the effect of wall cooling, the motion of the fluid through the lattice structures might effectively reduce the Soret effect, which is considered to be an important factor for FB in hydrogen combustion [39, 29].

The following sections address the third potential mechanism of whether lattice structures modify the flow dynamics to impact the FB behavior or the flow field. Starting point are the flow dynamics in the mixing duct.

2.3 Mixing duct flow

Numerical studies by Wang et al. [26] have demonstrated that flow instabilities in the mixing duct region of jet flame burners influence the resulting flow field and flame stability. Garnaud et al. [4] reported the origin of flow structures in the wall boundary layer of a non-reacting jet.

Since optical access is not possible with the lattice structures, pressure measurements were used to assess effects related to the lattice structures and the onset of FB. Figure 11 a) shows the power spectral density (PSD) calculated for the five pressure sensors p1 to p5 along the mixing duct.

The power spectra of the five sensors show the amplitude decreasing from upstream (p5) to downstream (p1), indicating a pressure node at the outlet of the mixing duct that might be related to a thermo-acoustic (TA) mode. No significant differences appeared across the different axial positions. Therefore, the subsequent analysis was focused on the sensor p5.

Reacting conditions at $T_{ad} = 1600$ K, shown in Fig. 11 b) by the black lines, displayed significant higher signal strength and altered spectral shape compared to non-reacting conditions indicated by the green lines. Higher frequencies (300 – 2000 Hz) were more promoted with flame and three significant peaks emerged at 468 Hz, 762 Hz, and 1440 Hz. A comparison with data at reacting conditions but without a quartz glass confinement (black dashed line) showed that reflections from the combustion chamber wall increased the spectral baseline for frequencies below approximately 600 Hz, making the peak at 468 Hz a possible TA mode. Consequently, the two peaks at 762 Hz and 1440 Hz were identified as flame-associated modes.

To assess the influence of the lattice structures, a stable operating point ($T_{ad} = 1500$ K, dashed lines) and an unstable point near FB ($T_{ad} = 1690$ K, solid lines) are compared in Fig. 12 for the nozzle N-950 and the machined variant. Both followed identical trends for the two flame conditions. With an increasing flame temperature, low-frequency pressure amplitudes decreased while high-frequency amplitudes increased. The frequency shift likely resulted from density changes at elevated temperatures and the related change in the speed of sound. This behavior was observed for all nozzle variants, but to varying degrees. A more comprehensive analysis can be found in App. A.

It can be concluded, that the pressure fluctuations in the mixing duct showed a distinct spectra with a peak at 468 Hz related to a TA mode and two peaks at 762 Hz and 1440 Hz related to the combustion process. Only the amplitudes of the latter ones were sensitive to flame temperature variations. An examination of the flow dynamics inside the combustion chamber and the influence of the TA mode on the combustion process are presented in the next section.

2.4 Flow dynamics in the combustion chamber

After examining the non-reacting flow in the mixing duct, the reacting flow in the combustion chamber was analyzed and assessed whether these flow dynamics influence FB beyond the assumed effect of wall cooling.

Figure 13 shows the first 30 SPOD eigenvalues for the machined nozzle at $T_{ad} = 1600$ K and inlet velocity $\bar{u}_x = 11.5$ m/s. A clear energy separation between the first two eigenvalues and the other modes was observed at frequencies of 100 – 200 Hz, corresponding to Strouhal numbers $St = (f * d)/\bar{u}_x$ of $St = 0.2 - 0.4$, based on the given nozzle diameter. The two leading modes exhibited comparable energy levels dominating the low-frequency domain, suggesting a classification as rank two. After peaks at 175 Hz, a monotonic decrease in the eigenvalue magnitude was observed for all modes ($j = 1 - 30$), indicating that low-frequency fluctuations dominated the flow field.

Since low-rank behavior of the two leading modes was observed across all nozzle variants, the analysis focused on the machined nozzle and the nozzle N-950. Figure 14 shows the leading eigenvalues $\lambda_\omega^{(1)}$ at adiabatic flame temperatures of 1400 K, 1600 K and directly before FB at $T_{ad} = 1840$ K. Panels a) and c) present the machined nozzle at inlet velocities of approximately 9 m/s and 11.5 m/s for stable conditions, respectively, while panels b) and d) show the same velocities for the nozzle N-950. For the unstable FB condition, the velocity was reduced to 11 m/s as described in Sec. 1.4. Because of the low mode energy above $f = 1000$ Hz observed in Fig. 13, the spectrum is truncated at this frequency to obtain a more detailed resolution.

Low-frequency dynamics dominated all SPOD spectra. With an increasing velocity, the low-frequency peak shifted to higher frequencies and became more broadband, while the energy content remained on a comparable level. In the high-frequency region, the increased velocity and flame temperature produced a less steep eigenvalue decay. This trend matches observations in the pressure spectra measured upstream in the mixing duct, see Fig. 12.

At $\bar{u}_x = 9$ m/s, a distinct peak appeared at 468 Hz, corresponding to a TA mode identified in the pressure measurements in Sec. 2.3. This mode was less pronounced in the lattice structure nozzle, which exhibited greater energy separation in the high-frequency region. This difference may result from increased small-scale turbulence generated by the nozzle wall structure which would match the observed reduction of the flame length in Fig. 5. However, the observed TA mode was very weak and showed no significant effect in the heat release spectra of the flame, an influence on the FB limits at the present operating conditions was assumed to be negligible. Overall, SPOD eigenvalues displayed broader frequency distributions with less pronounced peaks than the corresponding pressure spectra in the mixing duct.

Figure 15 illustrates the mode structure, showing the real part of the $j = 1$ eigenmode at $f = 171$ Hz (marked by triangles in panels c) and d) of Fig. 14). The left panels, a) and c), present data at $T_{ad} = 1600$ K, while the right panels, b) and d), show conditions directly before the FB at $T_{ad} = 1840$ K.

With a Strouhal number of $St = 0.3$, the mode reconstruction in panel a) reveals the axisymmetric component of a Kelvin-Helmholtz instability, while the non-symmetric component is located in the $j = 2$ sub-leading mode (not shown). For the nozzle N-950 under identical conditions, the non-symmetric part projected more strongly onto the leading mode. The KH instability originated at the mixing duct outlet, with multiple phase reversals occurring along the shear layer

in the downstream direction.

An increasing heat release toward higher flame temperatures enlarged the jet opening angle, particularly at the flame root near the mixing duct outlet (panels b) and d) near FB). This correlates with a stronger and more extensive recirculation, covering a larger fraction of the combustion chamber and extending toward the burner plate. Enhanced recirculation established an increased heat flux toward the burner plate, additionally explaining the pronounced increase in the burner rim temperature approaching FB conditions (Fig. 9).

The results indicate that the flow dynamics in the combustion chamber were dominated by large-scale coherent structures in the shear layer, specifically KH instabilities. This corresponds to the observation made for the low-frequency range in the mixing duct flow with the increasing shear layer thickness affecting the FB behavior. As the flame temperature increased, the KH mode shifted to slightly higher frequencies and the energy contained in high-frequency modes grew. With the porous wall structure, turbulence was further enhanced, while a TA mode observed at $f = 468$ Hz was damped. However, a specific influence of the lattice structures on the flow dynamics that affects the FB propensity was not observed.

3 Conclusion

This study demonstrates that incorporating BCC lattice structures into nozzles mitigates flame flashback in a hydrogen jet burner and further investigates the mechanisms underlying this effect. A comprehensive experimental characterization was conducted, combining flow measurements, flame imaging, and spectral analysis. Based on the observations, it is concluded that the primary mitigation mechanism is passive wall cooling by fresh gases flowing through the lattice structures with the cell size being related to this effect. Other potential mechanisms for the observed FB behavior were thoroughly discussed and ruled out based on experimental findings and literature data.

Analysis of the temperature data confirmed that wall temperature was the controlling parameter governing the FB limits across the different investigated nozzle configurations. The AM nozzle N-950 achieved a FB resistance significantly higher than the solid-wall AM nozzle and comparable to a reference nozzle with 25% higher thermal conductivity. This demonstrated that lattice structure optimization enables a broader operating range. Following the findings of [17, 41], that an increased heat transfer of the wall correlates with a decreased FB risk, it is reasonable to assume that the presumed mechanism of passive wall cooling is transferable to other nozzle materials.

Flow field measurements showed only minor modifications resulting from incorporating lattice structures in the nozzle wall, preserving general jet characteristics while in the flame images a reduction of the flame length with increasing pore size was observed. SPOD revealed dynamic differences, with the Kelvin-Helmholtz instability dominating low-frequency dynamics, increased asymmetry in the lattice-structured nozzle, and an enhanced turbulence generation.

The findings confirmed that the integration of lattice structures through AM provides a viable strategy for hydrogen FB mitigation by manipulating the coupled interaction between the flame and the thermal conditions of the wall. Future work should address the transferability to gas turbine relevant conditions in a multi-nozzle system, where elevated temperatures and flame-to-flame interactions may alter single-nozzle observations. Furthermore, the systematic optimization of the lattice structure in relation to operating conditions, combined with thermal management strategies, could further enhance the FB resistance.

Acknowledgments

This work has been conducted as part of the joint research project ENERGIZE (Adjoint-based and additive manufacturing-enabled optimization of hydrogen combustion systems) within the scope of the SPP2419 HyCAM and is supported by the German Research Foundation (DFG) under grant numbers 523881008, 530442286. Furthermore, the authors would like to thank Stefan Buchwald for his support at the measurements.

A Pressure fluctuations in the mixing duct flow

To isolate the effects of the bulk velocity and the flame temperature on the pressure fluctuations p' in the mixing duct, the pressure fluctuations were averaged and normalized by the total energy p'_{\max} in both the low-frequency (0 – 300 Hz) and the high-frequency (300 – 2000 Hz) ranges, shown in Fig. A1. The frequency separation at $f = 300$ Hz is based on the observations made in Fig. 12. The flame temperature is indicated by the color coding.

Results for the stable operating points ($T_{\text{ad}} = 1500$ K) appear in the panels a) and c), while the unstable points ($T_{\text{ad}} = 1690$ K) are shown in the panels b) and d). With an increase of the flame temperature the pressure amplitude decreases in the low-frequency range and increases in the high-frequency range, indicating the frequency shift observed in Fig. 12. The intense of pressure fluctuations might be affected by the wall turbulence and the flame temperature. This effect is least prominent for the solid AM nozzle with the smallest difference of pressure amplitude between both frequency ranges.

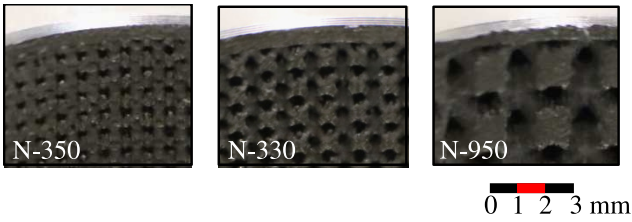


Figure 1: Close-ups of the porous walls with the solid plate at the nozzle outlet visible in the upper part of the images

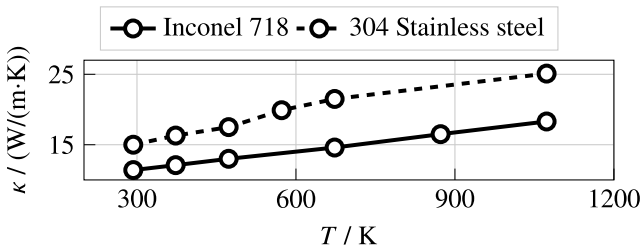


Figure 2: Thermal conductivity κ of Inconel 718 (solid line) and 304 stainless steel (1.4301) (dashed line) with increasing temperature

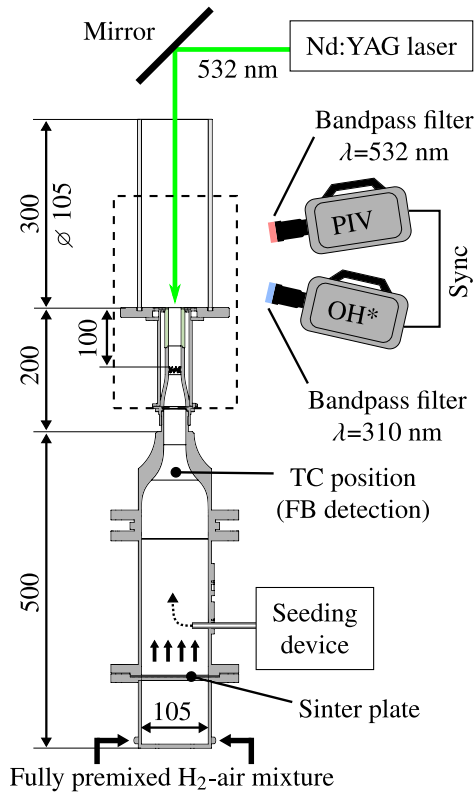


Figure 3: Test rig with the optical measurement setup. The flow direction is from bottom to top and all length scales are given in mm.

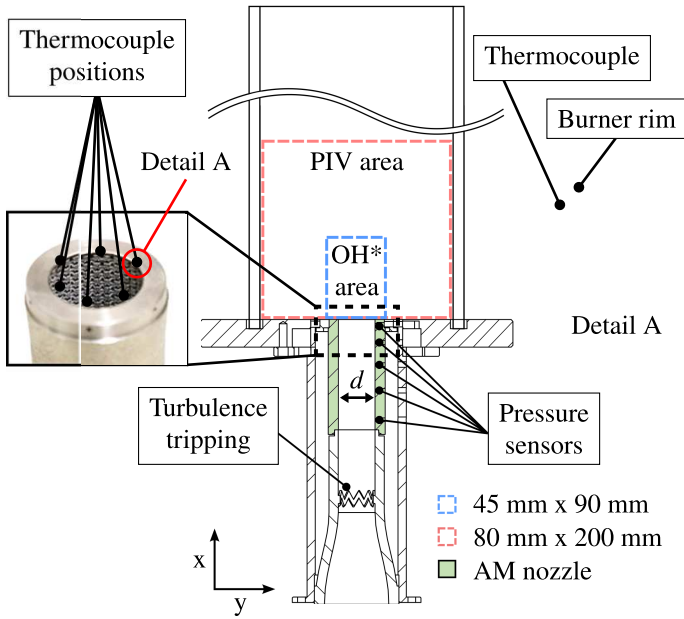


Figure 4: Detailed cross-section of the jet burner with the mixing duct and the changeable nozzle section of outlet diameter $d = 20$ mm (highlighted in green). In Detail A, the mounting situation of the thermocouple at the burner rim is depicted.

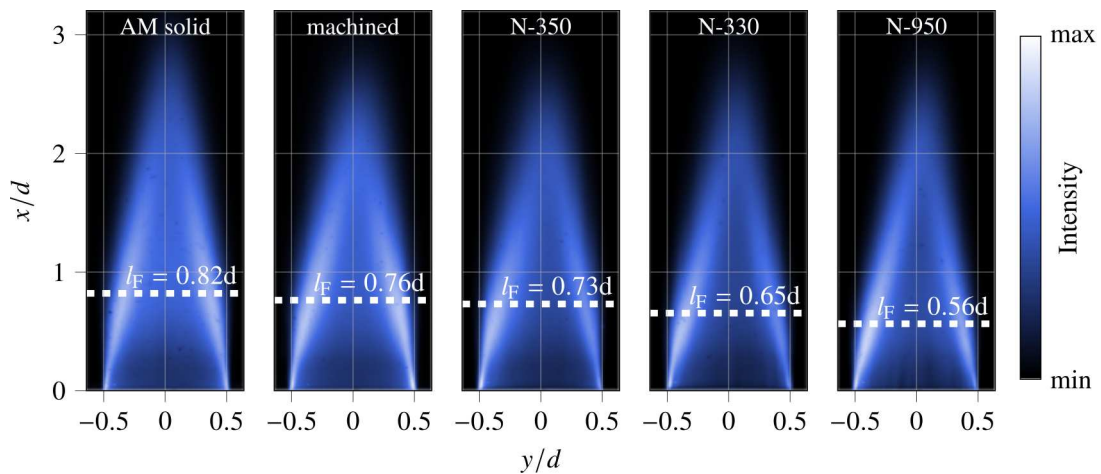


Figure 5: OH^* -chemiluminescence flame images at an adiabatic flame temperature of $T_{\text{ad}} = 1600$ K and an inlet velocity of $\bar{u}_x = 11.5$ m/s. The flame length l_F was determined by the maximum of the mean intensity along the y -axis.

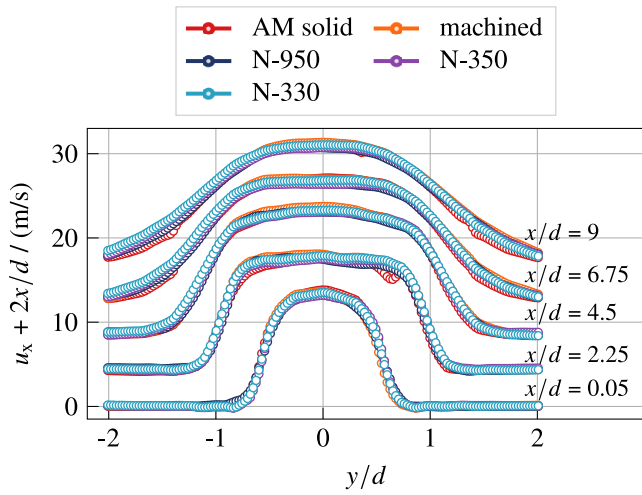


Figure 6: Axial velocity component \bar{u}_x shown at the axial positions x/d in the downstream direction over the combustion chamber width y/d . The operating condition was at an adiabatic flame temperature of $T_{\text{ad}} = 1600$ K and an inlet velocity of $\bar{u}_x = 11.5$ m/s.

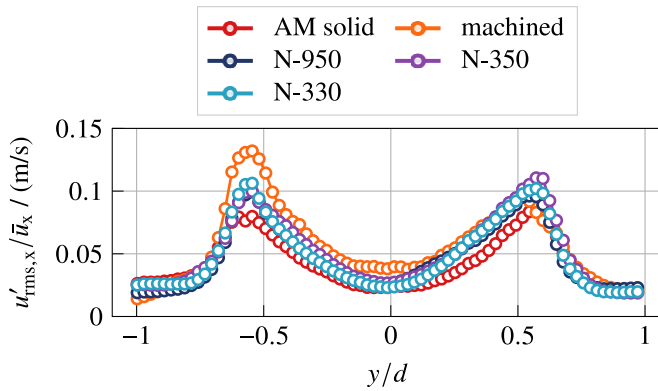


Figure 7: Turbulence intensity of the axial velocity component downstream of the nozzle outlet at $y/d = 0.05$ shown at the same operating condition as in Fig. 6.

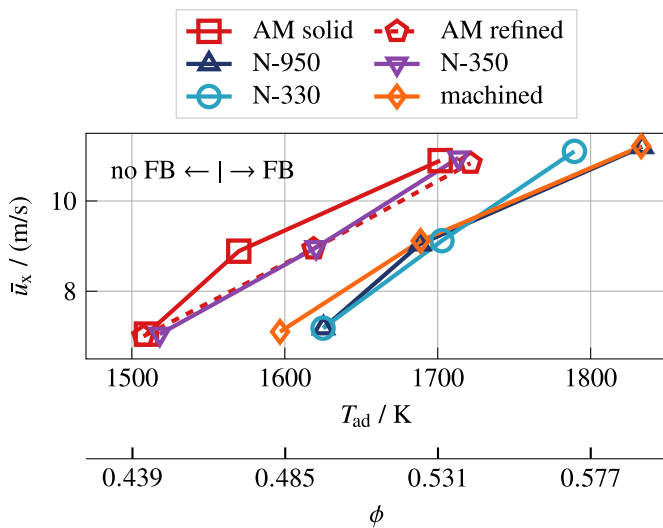


Figure 8: Flashback limits with the inlet velocity of the unburnt gas mixture \bar{u}_x as a function of the calculated adiabatic flame temperature, or equivalence ratio. A flashback is indicated by passing the linear interpolated solid lines from left to right.

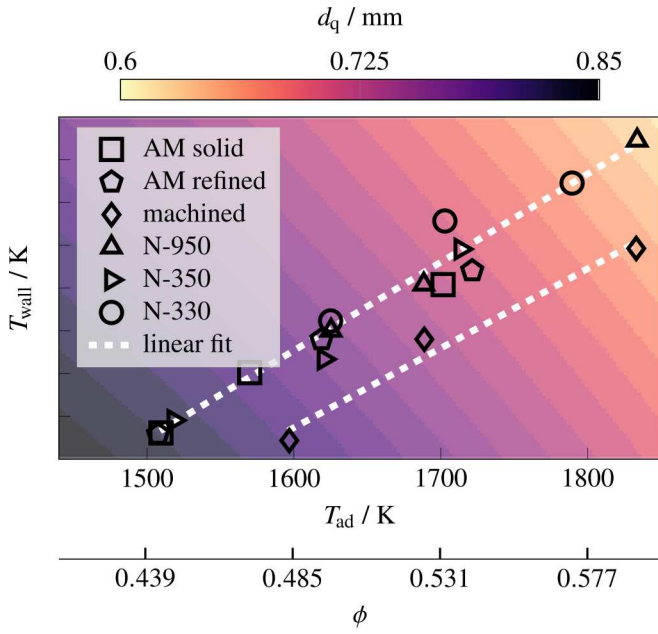


Figure 9: Measured wall temperatures (black marker) at the mixing duct outlet as a function of the calculated adiabatic flame temperature, or equivalence ratio. All measurement points are close to the FB condition. The background color depicts the associated quenching distance d_q , calculated based on [36].

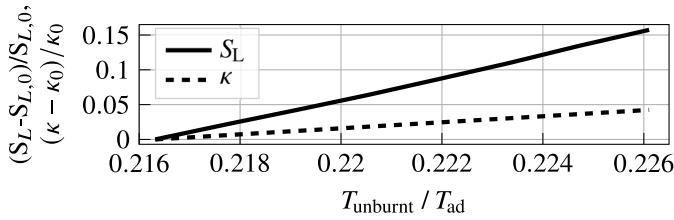


Figure 10: Effect of an inlet temperature variation ($\Delta T_{\text{unburnt}} = 20$ K) of the unburnt gas mixture on the laminar flame speed S_L and the thermal conductivity of unburnt gas κ . Both quantities are normalized by their respective initial conditions $S_{L,0}$ and κ_0 at $T_{\text{unburnt}} = 360$ K.

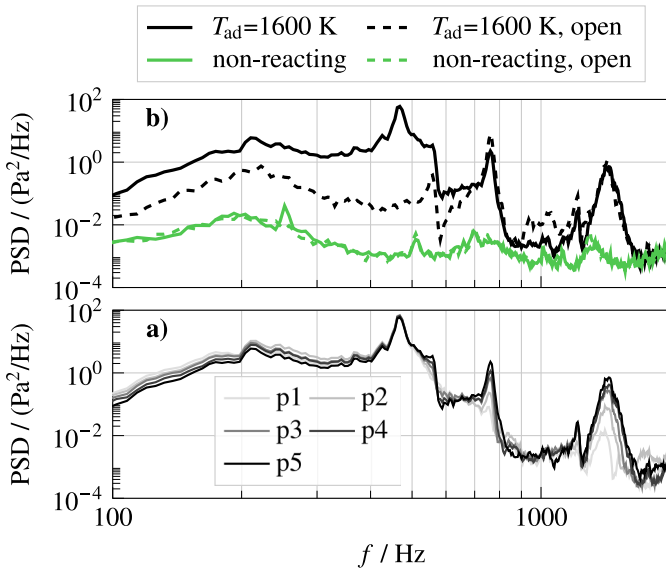


Figure 11: PSD of the machined nozzle at $\bar{u}_{\text{bulk}} = 9$ m/s. The bottom plot shows the signals of the five axial measurement positions (p1 to p5). Line brightness decreases with increasing distance to the mixing duct outlet. The top plot shows the PSD of pressure sensor p5 for the non-reacting cases (green lines) and the cases with flame at $T_{\text{ad}} = 1600$ K (black lines) both with (solid lines) and without (dashed lines) confinement.

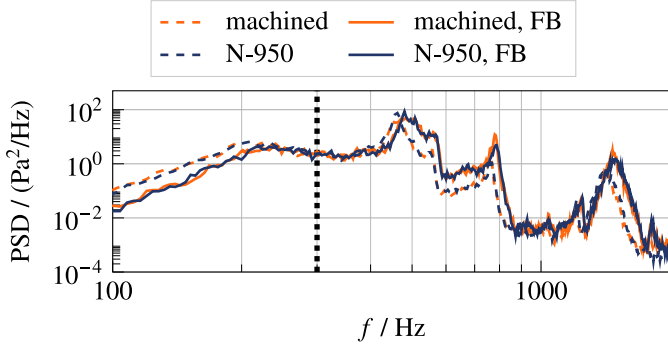


Figure 12: Power spectra of the machined nozzle and the nozzle N-950 at a bulk velocity of $\bar{u}_x = 9$ m/s. Both cases are depicted at $T_{ad} = 1500$ K (dashed lines) and $T_{ad} = 1690$ K (solid lines). The latter measurement point is measured over the last three seconds before a FB occurred. The dotted black line indicates $f = 300$ Hz.

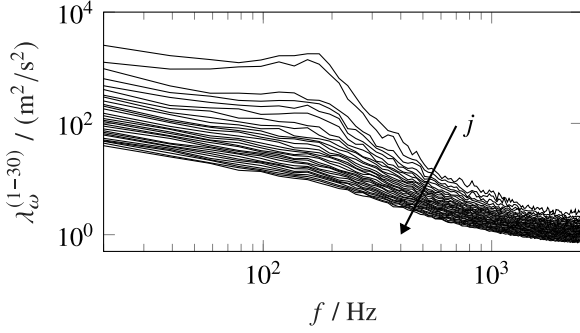


Figure 13: SPOD modes $j = 1 - 30$ calculated from the PIV data. Shown is the machined case for $\bar{u}_x = 11.5$ m/s at a flame temperature of $T_{ad} = 1600$ K.

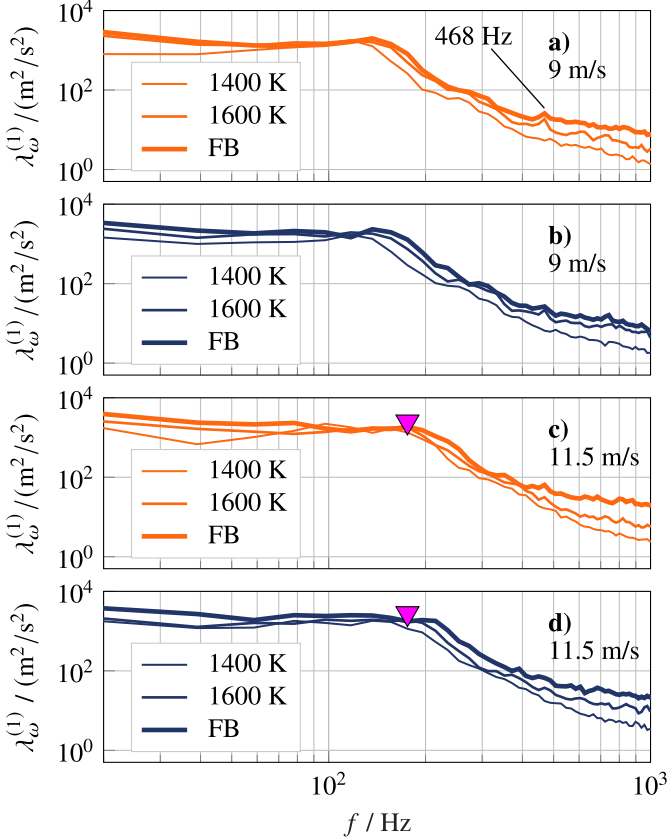


Figure 14: Leading SPOD modes for the machined nozzle (orange lines) and the nozzle N-950 (blue lines). FB shows the measurement point directly before flashback at the reduced bulk velocity of 11 m/s (thickest lines). Markers indicate the frequencies of the mode plots in Fig. 15.

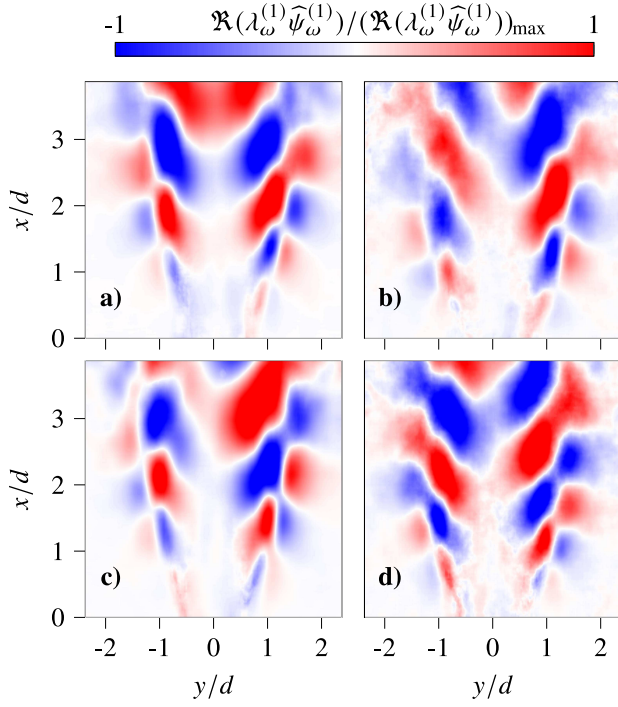


Figure 15: Real part of the leading SPOD mode at $f = 171$ Hz indicated in Fig. 14. Panels a) and c) show the stable operating points and panels b) and d) the moment directly before flashback.

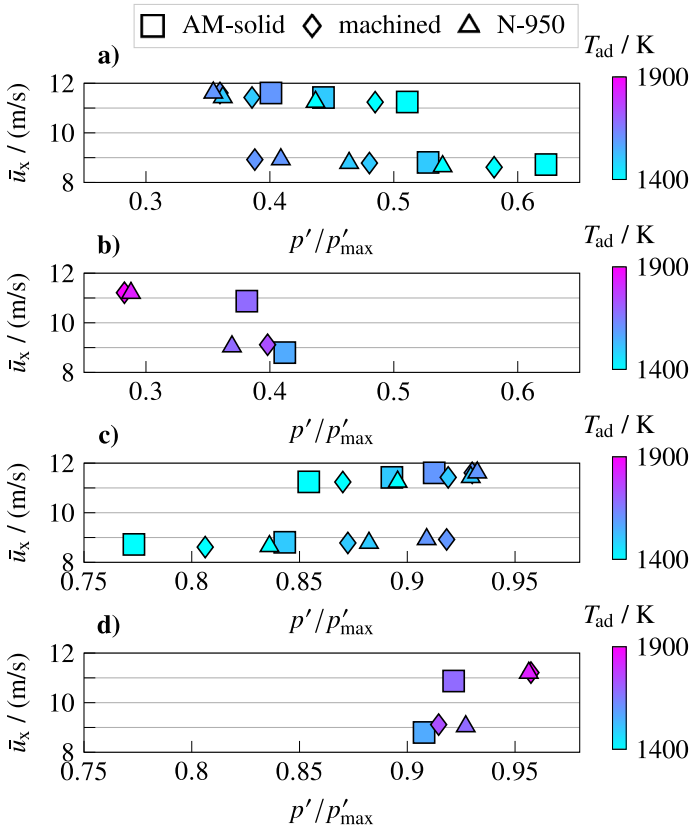


Figure A 1: Normalized pressure amplitudes for the two spectra regions below and above $f = 300$ Hz. Panels a) and b) show the low-frequency range (0 – 300 Hz) of the pressure fluctuations and panels c) and d) show the high-frequency range (300 – 2000 Hz) of the pressure fluctuations. Panels a) and c) are at stable operating conditions and panels b) and d) close to FB.

References

- [1] Guenther von Elbe and Morris Mentser. “Further Studies of the Structure and Stability of Burner Flames”. In: *J. Chemical Phys.* (1945).
- [2] H. Fellouah, C.G. Ball, and A. Pollard. “Reynolds number effects within the development region of a turbulent round free jet”. In: *International Journal of Heat and Mass Transfer* 52.17 (2009). ISSN: 0017-9310. DOI: <https://doi.org/10.1016/j.ijheatmasstransfer.2009.03.029>.
- [3] Christian Eichler, Georg Baumgartner, and Thomas Sattelmayer. “Experimental Investigation of Turbulent Boundary Layer Flashback Limits for Premixed Hydrogen-Air Flames Confined in Ducts”. In: *J. Eng. Gas Turb. Power* (2011). DOI: 10.1115/1.4004149.
- [4] X. Garnaud et al. “The preferred mode of incompressible jets: linear frequency response analysis”. In: *Journal of Fluid Mechanics* 716 (2013). DOI: 10.1017/jfm.2012.540.
- [5] Zhixuan Duan et al. “Influence of Burner Material, Tip Temperature, and Geometrical Flame Configuration on Flashback Propensity of H₂-Air Jet Flames”. In: *J. Eng. Gas Turb. Power* (2014). DOI: 10.1115/1.4025359.
- [6] Georg Baumgartner, Lorenz R. Boeck, and Thomas Sattelmayer. “Experimental Investigation of the Transition Mechanism From Stable Flame to Flashback in a Generic Premixed Combustion System With High-Speed Micro-Particle Image Velocimetry and Micro-PLIF Combined With Chemiluminescence Imaging”. In: *Journal of Engineering for Gas Turbines and Power* 138.2 (Sept. 2015). ISSN: 0742-4795. DOI: 10.1115/1.4031227.
- [7] Alireza Kalantari, Elliot Sullivan-Lewis, and Vincent McDonell. “Flashback Propensity of Turbulent Hydrogen–Air Jet Flames at Gas Turbine Premixer Conditions”. In: *Journal of Engineering for Gas Turbines and Power* 138.6 (Nov. 2015). ISSN: 0742-4795. DOI: 10.1115/1.4031761.
- [8] Vera Hoferichter, Christoph Hirsch, and Thomas Sattelmayer. “Analytic prediction of unconfined boundary layer flashback limits in premixed hydrogen–air flames”. In: *Combustion Theory and Modelling* 21.3 (2017). DOI: 10.1080/13647830.2016.1240832.
- [9] Alireza Kalantari and Vincent McDonell. “Boundary layer flashback of non-swirling premixed flames: Mechanisms, fundamental research, and recent advances”. In: *Progress in Energy and Combustion Science* 61 (2017). ISSN: 0360-1285. DOI: <https://doi.org/10.1016/j.pecs.2017.03.001>.
- [10] David G Goodwin et al. “Cantera: An object-oriented software toolkit for chemical kinetics, thermodynamics, and transport processes”. In: *Zenodo* (2018).
- [11] Hidemasa Kosaka et al. “Wall heat fluxes and CO formation/oxidation during laminar and turbulent side-wall quenching of methane and DME flames”. In: *International Journal of Heat and Fluid Flow* 70 (2018). ISSN: 0142-727X. DOI: <https://doi.org/10.1016/j.ijheatfluidflow.2018.01.009>.

-
- [12] Andrea Ciani et al. “Superior fuel and operational flexibility of sequential combustion in Ansaldo Energia gas turbines”. In: *Journal of the Global Power and Propulsion Society* 3 (2019). DOI: 10.33737/jgpps/110717.
- [13] Y. Kuwata, K. Tsuda, and K. Suga. “Direct numerical simulation of turbulent conjugate heat transfer in a porous-walled duct flow”. In: *Journal of Fluid Mechanics* 904 (2020). DOI: 10.1017/jfm.2020.669.
- [14] Rikard Magnusson and Mats Andersson. “Operation of SGT-600 (24 MW) DLE Gas Turbine With Over 60 % H₂ in Natural Gas”. In: *Turbo Expo: Power for Land, Sea, and Air Volume 9: Oil and Gas Applications; Organic Rankine Cycle Power Systems; Steam Turbine* (Sept. 2020). DOI: 10.1115/GT2020-16332.
- [15] S. Schmidt and K. Oberleithner. “Instability of forced planar liquid jets: mean field analysis and nonlinear simulation”. In: *Journal of Fluid Mechanics* 883 (2020), A7. DOI: 10.1017/jfm.2019.855.
- [16] Kazuhiko Suga, Yuki Okazaki, and Yusuke Kuwata. “Characteristics of turbulent square duct flows over porous media”. In: *Journal of Fluid Mechanics* 884 (2020). DOI: 10.1017/jfm.2019.914.
- [17] Shuyu Ding et al. “Numerical study of the influence of wall roughness on laminar boundary layer flashback”. In: *Phys. Rev. Fluids* 6 (2 Feb. 2021). DOI: 10.1103/PhysRevFluids.6.023201.
- [18] I. Gibson et al. *Additive Manufacturing Technologies*. Engineering. Springer Cham, 2021. ISBN: 9783030561260. DOI: <https://doi.org/10.1007/978-3-030-56127-7>.
- [19] Andrea Gruber et al. “Direct Numerical Simulation of hydrogen combustion at auto-ignitive conditions: Ignition, stability and turbulent reaction-front velocity”. In: *Combustion and Flame* 229 (2021), p. 111385. ISSN: 0010-2180. DOI: <https://doi.org/10.1016/j.combustflame.2021.02.031>.
- [20] Ukhwa Jin and Kyu Tae Kim. “Experimental investigation of combustion dynamics and NO_x/CO emissions from densely distributed lean-premixed multinozzle CH₄/C₃H₈/H₂/air flames”. In: *Combustion and Flame* 229 (2021). ISSN: 0010-2180. DOI: <https://doi.org/10.1016/j.combustflame.2021.111410>.
- [21] Hyebin Kang and Kyu Tae Kim. “Combustion dynamics of multi-element lean-premixed hydrogen-air flame ensemble”. In: *Combustion and Flame* 233 (2021). ISSN: 0010-2180. DOI: <https://doi.org/10.1016/j.combustflame.2021.111410>.
- [22] David Noble et al. “Assessment of Current Capabilities and Near-Term Availability of Hydrogen-Fired Gas Turbines Considering a Low-Carbon Future”. In: *Journal of Engineering for Gas Turbines and Power* 143.4 (Feb. 2021). ISSN: 0742-4795. DOI: 10.1115/1.4049346.
- [23] Thorsten Zirwes et al. “Numerical Study of Quenching Distances for Side-Wall Quenching Using Detailed Diffusion and Chemistry”. In: *Flow, turbulence and combustion* 106 (2021). ISSN: 1386-6184, 1573-1987. DOI: 10.1007/s10494-020-00215-0.
- [24] Lukas Berger, Antonio Attili, and Heinz Pitsch. “Synergistic interactions of thermodiffusive instabilities and turbulence in lean hydrogen flames”. In: *Combustion and Flame* 244 (2022). ISSN: 0010-2180. DOI: <https://doi.org/10.1016/j.combustflame.2022.112254>.
- [25] Bernhard Čosić et al. “Experimental and Numerical Advancement of the MGT Combustor Towards Higher Hydrogen Capabilities”. In: *Turbo Expo: Power for Land, Sea, and Air Volume 3B: Combustion, Fuels, and Emissions* (2022). DOI: 10.1115/GT2022-82110.

-
- [26] Chuhan Wang et al. “Linear instability of a premixed slot flame: Flame transfer function and resolvent analysis”. In: *Combustion and Flame* 240 (2022). ISSN: 0010-2180. DOI: <https://doi.org/10.1016/j.combustflame.2022.111111>.
- [27] Jan Paul Beuth et al. “Thermoacoustic Characterization of a Premixed Multi Jet Burner for Hydrogen and Natural Gas Combustion”. In: *Journal of Engineering for Gas Turbines and Power* 146.4 (Dec. 2023). DOI: 10.1115/1.4063692.
- [28] Alexander Jaeschke et al. “Experimental Investigation of a Multi Tube Burner for Premixed Hydrogen and Natural Gas Low Emission Combustion”. In: *Journal of Engineering for Gas Turbines and Power* 145.12 (Oct. 2023). ISSN: 0742-4795. DOI: 10.1115/1.4063378.
- [29] Filippo Fruzza et al. “The importance of Soret effect, preferential diffusion, and conjugate heat transfer for flashback limits of hydrogen-fueled perforated burners”. In: *Proceedings of the Combustion Institute* 40 (2024). ISSN: 1540-7489. DOI: <https://doi.org/10.1016/j.proci.2024.105581>.
- [30] Sebastian Hermeth et al. “100% H₂ DLE Gas Turbine Combustion Technology Platform Development”. In: *Proceedings of ASME Turbo Expo 2024*. Turbo Expo: Power for Land, Sea, and Air Volume 3B: Combustion, Fuels, and Emissions (June 2024). DOI: 10.1115/GT2024-128517.
- [31] Ianos Psomoglou et al. “Influence of AM Generated Burner Surface Roughness on NO_x Emissions and Operability of Hydrogen-Rich Fuels”. In: *Combustion Science and Technology* (2024). DOI: 10.1080/00102202.2024.2390666.
- [32] Francesco G. Schiavone et al. “On the adequacy of OH* as heat release marker for hydrogen–air flames”. In: *Proceedings of the Combustion Institute* 40.1 (2024). ISSN: 1540-7489. DOI: <https://doi.org/10.1016/j.proci.2024.105581>.
- [33] Haiqin Zhou et al. “Hydrogen-fueled gas turbines in future energy system”. In: *International Journal of Hydrogen Energy* 64 (2024). ISSN: 0360-3199. DOI: <https://doi.org/10.1016/j.ijhydene.2024.03.327>.
- [34] Holger Ax et al. “Investigation of Critical Operating Conditions for Hydrogen Flames Under Typical Gas Turbine Conditions”. In: *Proceedings Turbo Expo*. Turbo Expo Volume 3A: Combustion, Fuels and Emissions (June 2025). DOI: 10.1115/GT2025-152427.
- [35] Alexander Jaeschke, Dominik Wassmer, and Christian Oliver Paschereit. “Influence of Variable Fuel Staging on the Flow Structures in a Multi-Jet Burner Operated on Lean-Premixed Hydrogen”. In: *Proceedings Turbo Expo*. Turbo Expo Volume 3B: Combustion, Fuels and Emissions (June 2025). DOI: 10.1115/GT2025-153254.
- [36] Tahsin Berk Kıymaz, Nijso Beishuizen, and Jeroen van Oijen. “Numerical analysis of quenching distance in laminar premixed hydrogen and methane flames”. In: *Fuel* 396 (2025). ISSN: 0016-2361. DOI: <https://doi.org/10.1016/j.fuel.2025.135111>.
- [37] Philipp Maximilian zur Nedden et al. “Investigation of Flashback Limits and Detection Strategies for Jet-Stabilized Hydrogen Flames”. In: *Proceedings Turbo Expo*. Turbo Expo Volume 3A: Combustion, Fuels and Emissions (June 2025). DOI: 10.1115/GT2025-152906.
- [38] Jaehyun Park and Kyu Tae Kim. “Boundary layer flashback limits and flame dynamics of turbulent premixed hydrogen-air flames”. In: *Combustion and Flame* 273 (2025). ISSN: 0010-2180. DOI: <https://doi.org/10.1016/j.combustflame.2025.111111>.

-
- [39] P. Porath et al. “Low velocity streaks combined with intrinsic flame instabilities provoke boundary layer flashback in a turbulent premixed jet-stabilized hydrogen flame”. In: *Combustion and Flame* 278 (2025). ISSN: 0010-2180. DOI: <https://doi.org/10.1016/j.combustflame.2025.114236>.
- [40] GE Vernova press release. *GE Vernova validates 100 percent hydrogen-fueled DLN combustor technology aiming to decarbonize its industrial B- and E-Class gas turbines, GE Vernova News*. <https://www.gevernova.com/news/dln-combustor-technology-aiming-6>. 2025. (Visited on 11/27/2025).
- [41] Robin Vivoli et al. “Surface Roughness Effects on the Operability and Performance of a Hydrogen Jet Burner”. In: *Journal of Engineering for Gas Turbines and Power* 148 (Oct. 2025). DOI: 10.1115/1.4069474.
- [42] Jakob G.R. von Saldern et al. “Low-frequency streaky structures in turbulent hydrogen jet flames”. In: *Combustion and Flame* 278 (2025). ISSN: 0010-2180. DOI: <https://doi.org/10.1016/j.combustflame.2025.114231>.
- [43] Gregory P. Smith et al. “GRI-Mech 3.0”. In: (). URL: http://www.me.berkeley.edu/gri_mech/.